Check for updates

ADVANCED MATERIALS
www.advmat.de

Néel-Type Elliptical Skyrmions in a Laterally Asymmetric Magnetic Multilayer

Baoshan Cui, Dongxing Yu, Ziji Shao, Yizhou Liu, Hao Wu, Pengfei Nan, Zengtai Zhu, Chuangwen Wu, Tengyu Guo, Peng Chen, Heng-An Zhou, Li Xi, Wanjun Jiang, Hao Wang, Shiheng Liang, Haifeng Du, Kang L. Wang, Wenhong Wang, Kehui Wu, Xiufeng Han, Guangyu Zhang, Hongxin Yang, and Guoqiang Yu**

Magnetic skyrmions, topological-chiral spin textures, have potential applications in next-generation high-density and energy-efficient spintronic devices for information storage and logic technologies. Tailoring the detailed spin textures of skyrmions is of pivotal importance for tuning skyrmion dynamics, which is one of the key factors for the design of skyrmionic devices. Here, the direct observation of parallel aligned elliptical magnetic skyrmions in Pt/Co/Ta multilayers with an oblique-angle deposited Co layer is reported. Domain wall velocity and spin–orbit-torque-induced out-of-plane effective field analysis demonstrate that the formation of unusual elliptical skyrmions is correlated to the anisotropic effective perpendicular magnetic anisotropy energy density (K_u^{eff}) and Dzyaloshinskii–Moriya interaction (DMI) in the film plane. Structural analysis and first-principles calculations further show that the anisotropic K_u^{eff} and DMI originate from the interfacial anisotropic strain introduced by the oblique-angle deposition. The work provides a method to tune the spin textures of skyrmions in magnetic multilayers and, thereby, a new degree of freedom for the design of skyrmionic devices.

Magnetic skyrmions, topological chiral spin textures, have aroused extensive research interests due to their intriguing topology-related physics and promising applications in spintronic devices.[1–4] In most cases, skyrmions' chiral spin textures are mainly determined by the Dzyaloshinskii–Moriya interaction (DMI),[5–7] which favors a non-collinear spin configuration between neighboring spins. The appearance of DMI is a direct consequence of spin-orbit coupling and inversion symmetry breaking.[8–10] Depending on the structural symmetry of materials, DMI favors spin arrangement with specific symmetries. For example, natural inversion symmetry breaking in single-crystal materials, such as MnSi,[11–13] FeCoSi,[14,15] FeGe,[16] and Cu_2OSeO_3,[17,18] leads to the emergence of bulk-type DMI

Dr. B. S. Cui, Dr. Z. T. Zhu, C. W. Wu, T. Y. Guo, P. Chen, Prof. W. H. Wang, Prof. K. H. Wu, Prof. X. F. Han, Prof. G. Y. Zhang, Prof. G. Q. Yu
Songshan Lake Materials Laboratory
Dongguan, Guangdong 523808, China
E-mail: guoqiangyu@iphy.ac.cn

Dr. B. S. Cui, Dr. Y. Z. Liu, Dr. Z. T. Zhu, Prof. W. H. Wang, Prof. K. H. Wu, Prof. X. F. Han, Prof. G. Y. Zhang, Prof. G. Q. Yu
Beijing National Laboratory for Condensed Matter Physics
Institute of Physics
Chinese Academy of Sciences
Beijing 100190, China

Dr. D. X. Yu, Dr. Z. J. Shao, Prof. H. X. Yang
Ningbo Institute of Materials Technology and Engineering
Chinese Academy of Sciences
Ningbo 315201, China
E-mail: hongxin.yang@nimte.ac.cn

Dr. Y. Z. Liu
RIKEN Center for Emergent Matter Science (CEMS)
Wako 351-0198, Japan

Dr. H. Wu, Prof. K. L. Wang
Department of Electrical and Computer Engineering
University of California
Los Angeles, CA 90095, USA

The ORCID identification number(s) for the author(s) of this article can be found under https://doi.org/10.1002/adma.202006924.

DOI: 10.1002/adma.202006924

P. F. Nan
Institutes of Physical Science and Information Technology
Anhui University
Hefei 230601, China

C. W. Wu, Prof. H. Wang, Prof. S. H. Liang
Faculty of Physics and Electronic Science
Hubei University
Wuhan 430062, China

Dr. H.-A. Zhou, Prof. W. J. Jiang
State Key Laboratory of Low-Dimensional Quantum Physics and Department of Physics
Tsinghua University
Beijing 100084, China

Prof. L. Xi
Key Laboratory for Magnetism and Magnetic Materials of Ministry of Education, School of Physical Science and Technology
Lanzhou University
Lanzhou 730000, China

Prof. H. F. Du
Anhui Province Key Laboratory of Condensed Matter Physics at Extreme Conditions
High Magnetic Field Laboratory of Chinese Academy of Sciences
University of Science and Technology of China
Hefei 230031, China

 © 2021 Wiley-VCH GmbH

and Bloch-type skyrmions. By constructing magnetic thin-film heterostructures, where the inversion symmetry is broken at the interface, interfacial DMI can also be artificially introduced without being in single-crystalline materials.[4] In this case, the thin-film heterostructures can be well described by a $C_{\infty v}$ symmetry and gives rise to a Néel-type skyrmion.[19–24]

The physical properties of skyrmions are determined by their detailed chiral spin textures together with the topology.[1,2] While most skyrmions exhibit equivalent topology, they may have different spin configurations, such as the Bloch- or Néel-type skyrmions.[2] Therefore, modification of the detailed spin textures of skyrmions could provide a new degree of freedom for studying the related physics and applications in addition to engineering their energetics and sizes. Since the chiral spin textures of skyrmions are closely related to the structural symmetry of the underlying materials, the skyrmion textures can be effectively modified by tuning the material structures. In single-crystal bulk magnetic materials or epitaxial magnetic films, detailed spin textures of skyrmions can be designed by choosing materials with specific symmetries and thus specific types of DMI. For example, Bloch-type skyrmions with a circular shape are usually observed in B20-type crystals.[11,15–17,25] Furthermore, elliptical skyrmions were reported in single-crystals and epitaxial films with certain symmetry breaking in the film plane.[26–30] More recently, antiskyrmions have also been successfully observed in non-centrosymmetric magnets with D_{2d} symmetry, in which the signs of DMI along two orthogonal in-plane directions are opposite.[31–36] On the other hand, as a promising candidate for skyrmionic applications, polycrystalline thin-film heterostructures that can be readily prepared by industry-friendly magnetron sputtering systems have the flexibility of engineering their magnetic properties.[37–40] However, an efficient way to engineer elliptical skyrmions and antiskyrmions in polycrystalline multilayer is still missing.

In this work, we report the observation of parallel aligned elliptical skyrmions in a sputtering-grown polycrystalline multilayer, in which the in-plane rotation symmetry is broken due to the oblique-angle deposition of the magnetic layer. The formation of elliptical skyrmions is found to be related to the anisotropic effective perpendicular magnetic anisotropy energy density (K_u^{eff}) and DMI in the film plane. The first-principles calculations reveal that these two anisotropies are originated from the interfacial anisotropic strain. Our results provide a route to tuning the symmetry of skyrmions for related physics study and device applications.

The film stacks consisting of Ta(2)/Pt(3)/Co(t_{Co})/Ta(2)/Pt(1) (thickness in nanometers) were grown by magnetron sputtering on a thermally oxidized Si/SiO_2 substrate under the base pressure lower than 5×10^{-8} Torr. The ferromagnetic Co layer was deposited by oblique-angle deposition and thus has a wedge shape, as shown in **Figure 1**a. The film has a perpendicular magnetic anisotropy (PMA), as manifested by the out-of-plane square hysteresis loops in Figure 1b. The coercivity shows a nonmonotonic dependence on the thickness (see Figure 1b), corresponding to the nonmonotonic variation of PMA, which has been well explained in previous works.[41,42] We first study the domain pattern in this symmetry-broken sample by magneto-optical Kerr effect (MOKE) microscopy in a polar configuration. Figure 1d–f shows the representative MOKE images of the magnetic domain patterns for different Co layer thickness. The observed domains in Figure 1d,e are created by applying the magnetic field pulse normal to the film (H_z). Interestingly, we find the shapes of the domains in the thin and thick regions are sharply different. In the thickness region with $t_{Co} > 1.30$ nm, the domains have a circular shape (Figure 1d), which is similar to the control sample with a uniform Co layer thickness (see Section S1, Supporting Information). By contrast, the nucleated magnetic domains have an elliptical shape in the region with 0.80 nm < t_{Co} < 1.30 nm. The elliptical domains also expand in an anisotropic manner under H_z, as shown by the extracted domain wall (DW) velocities (v) for x and y axes (Figure 1c). The velocities for x and y axes exhibit an obvious difference ($\Delta v = v_x - v_y$), and Δv fades with t_{Co} increasing. Δv eventually disappears with increasing Co layer thickness, indicating the interfacial origin of the formation of elliptical domains.

The shape deformation becomes even stronger for $t_{Co} < 0.80$ nm. All the domains are elongated along the x axis, as shown in Figure 1f. In this thickness region, the film cannot sustain a single magnetic domain at zero field due to the reduced PMA. As H_z increases, the stripe-domains gradually transform into isolated elongated domains,[43] featuring the parallel alignment along x axis (see Figure 1g,h). Because of the strong DMI in this system, domain walls have a Néel-type chiral spin texture.[44,45] The elongated domains eventually evolve into smaller elliptical skyrmions with increasing field, as shown in Figure 1i. The inset shows a 2.8×1.7 μm^2 zoom of an elliptical skyrmion, the size of the elliptical skyrmion is about 1.8×0.8 μm. It is worth noting that the micrometer-sized elliptical skyrmion is not a compact skyrmion since there is a magnetization plateau in its center. Based on the definition of topological charge $N = \int\int d^2r \mathbf{m} \cdot (\partial_x \mathbf{m} \times \partial_y \mathbf{m})/4\pi$,[2] where $\mathbf{m}$ is the unit magnetization vector, the topological charge of a circular skyrmion is calculated to be +1 or −1. The topological charge of an elongated domain or an elliptical skyrmion is also +1 or −1.[46,47] Therefore, the circular skyrmion, elongated domain, and elliptical skyrmion are topologically equivalent. Besides, the elliptical skyrmions with smaller size and higher density can be observed in the region with $t_{Co} < 0.75$ nm, but it is challenging to image using our MOKE system due to the thermally driven appearance, disappearance, and Brownian dynamics[48] during capturing the images (see Video S1, Supporting Information).

To understand the origin of the elliptical domains and skyrmions, we first discuss the origin of the anisotropic DW motion. For the DW motion, the velocity is determined by the DW energy density (σ),[49,50] which can be expressed as $\sigma = \sigma_0 + 2K_D\Delta - \pi\Delta\mu_0 M_s|H_{DMI}|$ for Néel-type DW,[51] where σ_0 is the Bloch wall energy density, K_D is the DW anisotropy energy density and keeps as a constant, Δ is the DW width ($\Delta = \sqrt{A/K_u^{eff}}$, A is the exchange constant), M_s is the saturation magnetization, and H_{DMI} is the intrinsic DMI field. Hence, the DW velocity is correlated to K_u^{eff} and H_{DMI}. In most of the studied sputtering-grown heterostructures, K_u^{eff} and H_{DMI} are isotropic, and hence the DW velocity is isotropic.[50,52,53] In our sample, the full rotation symmetry is broken due to the oblique-angle deposition, and hence we speculate that K_u^{eff} and H_{DMI} may become anisotropic due to the symmetry breaking, which will be demonstrated in the following.

Figure 2a shows the in-plane magnetic hysteresis loops for $t_{Co} \approx 0.85$ nm measured by a superconducting quantum

© 2021 Wiley-VCH GmbH

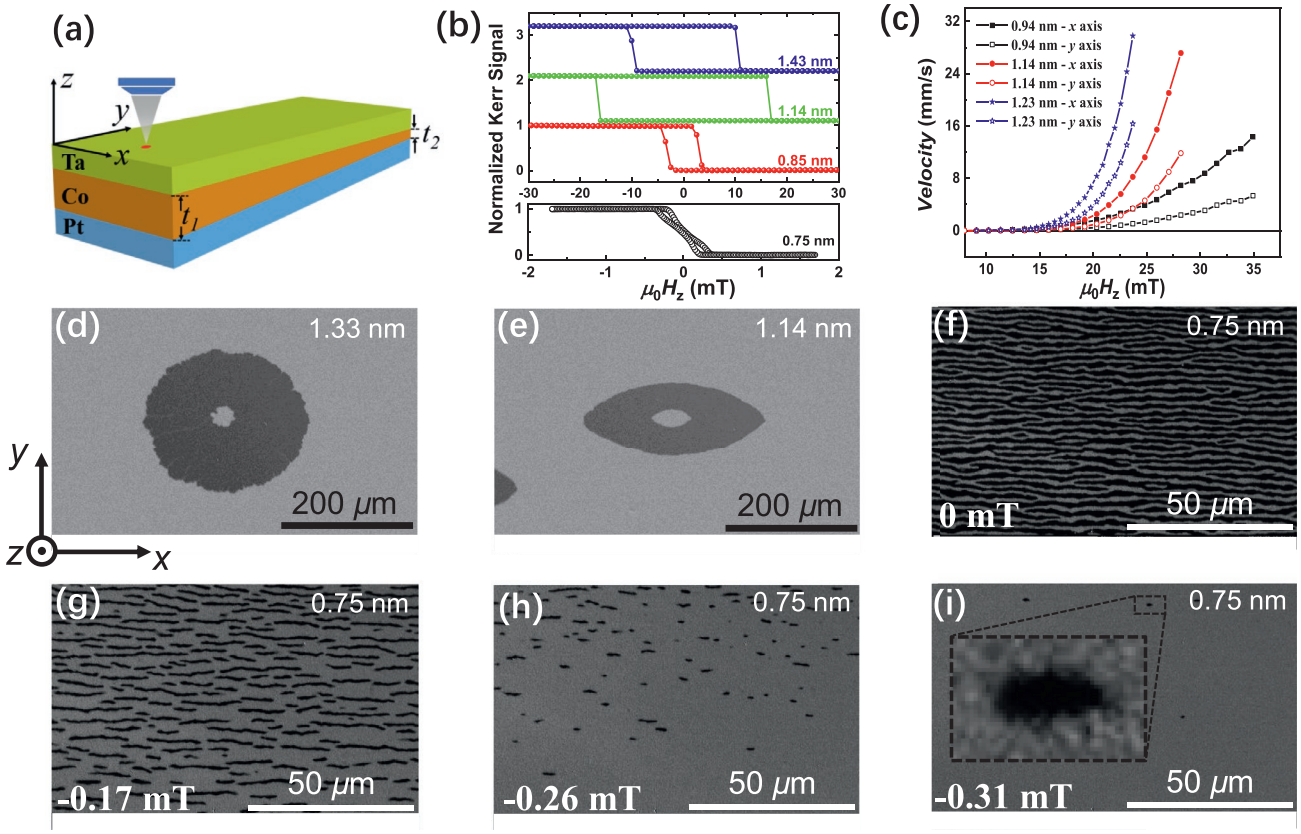

Figure 1. a) Schematic of the polar MOKE measurements, in which the wedge direction is parallel to *y* axis. b) Hysteresis loops for different Co thicknesses measured by MOKE microscopy. c) DW velocity for *x* and *y* axes as a function of the out-of-plane magnetic field for different Co thicknesses. d,e) MOKE images for different Co thicknesses after the application of magnetic field pulses. For getting images (d) and (e), an out-of-plane magnetic field pulse was first applied to nucleate a reverse domain, corresponding to the central region with bright color. This initial state was recorded as a reference background. Then, another out-of-plane magnetic field pulse was applied to drive the DW propagation outwards. The image is obtained by capturing the final state and subtracting the reference background. f–i) MOKE images of DW patterns under different out-of-plane external fields with $t_{Co} = 0.75$ nm. The insert of (i) exhibits a 2.8×1.7 μm^2 zoom of an elliptical skyrmion.

interfere device (SQUID). The saturation fields for *x* and *y* axes are distinctly different, indicating the existence of the anisotropic K_u^{eff} in the film plane. The PMA for the two axes can be extracted by integrating the close area surrounded by the out-of-plane (Figure 1b) and in-plane (Figure 2a) hysteresis loops. The K_u^{eff} values for *x* and *y* axes are determined to be $K_{ux}^{eff} \approx 2.68 \times 10^5$ J m^{-3} and $K_{uy}^{eff} \approx 1.75 \times 10^5$ J m^{-3}, respectively. We define this feature of K_u^{eff} as anisotropic K_u^{eff}. By contrast, K_u^{eff} is isotropic for the region with a thicker Co layer (see Section S3, Supporting Information). The DMI effective fields (H_{DMI})

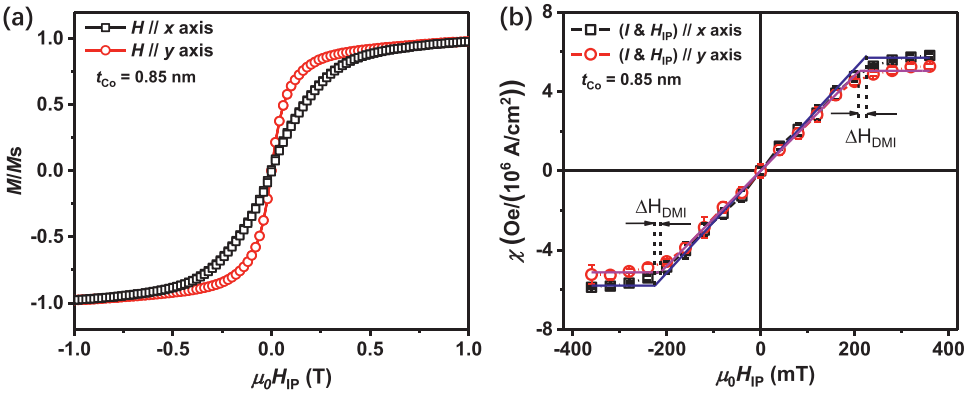

Figure 2. a) Hysteresis loops for the wedged thin film with $t_{Co} = 0.85$ nm measured by SQUID. The in-plane magnetic fields (H_{IP}) are applied along *x* and *y* axes. b) Current-induced out-of-plane effective field per current density ($\chi = H_{eff}\, z/J_e$) as a function of in-plane bias field for $t_{Co} = 0.85$ nm. The solid lines are the best fitting curves. The black squares and red circles represent the data with the current and in-plane magnetic fields are collinearly applied along *x* (*I* and H_{IP}//*x* axis) and *y* (*I* and H_{IP}//*y* axis) axes, respectively.

© 2021 Wiley-VCH GmbH

Table 1. Summary of the magnetic parameters and obtained effective DMI constant $|D|$ for x and y axes for the wedged sample with $t_{Co} = 0.85$ nm. M_s, K_u^{eff}, Δ, and $|H_{DMI}|$ represent the saturation magnetization, effective perpendicular magnetic anisotropy energy density, DW width, and DMI effective field, respectively. Exchange constant $A = 1.6 \times 10^{-11}$ J m^{-1} is used for calculating the Δ.

	x axis	y axis
M_s [emu cc^{-1}]	1092	1092
K_u^{eff} [J m^{-3}]	2.68×10^5	1.75×10^5
Δ [nm]	7.73	9.56
$\lvert H_{DMI}\rvert$ [T]	0.2248	0.2122
$\lvert D\rvert$ [mJ m^{-2}]	1.898	2.215

for x and y axes can also be extracted by spin–orbit torque (SOT)-induced hysteresis loop shift measurements.[54–56] We summarized the SOT-induced out-of-plane effective field (H_z^{eff}) per current density (J_e) (i.e., $\chi = H_z^{eff}/J_e$) as a function of in-plane magnetic field (H_{IP}) for $t_{Co} = 0.85$ nm in Figure 2b. χ is saturated at different values for x and y axes, corresponding to the values of H_{DMI}. The DMI constant can then be calculated by $|D| = \mu_0 M_s \Delta |H_{DMI}|$.[44,54] **Table 1** summarizes the magnetic parameters and obtained $|D|$ values for x and y axes. Clearly, the $|D|$ values are different for x and y axes, indicating the existence of the DMI anisotropy in the film plane. Analogous to the anisotropic K_u^{eff}, the DMI anisotropy gradually disappears with increasing Co layer thickness, as discussed in Section S3, Supporting Information. Hence, the anisotropic K_u^{eff} and DMI are responsible for the anisotropic domain wall motion and can also be the origin of the formation of elliptical domains and skyrmions.

To further verify the correlation, Monte Carlo simulations with the standard Metropolis algorithm were performed on the formation of skyrmion.[57,58] In the calculation of energy terms of the Hamiltonian, the simulated ultrathin square ferromagnetic film with a side length of 225 nm and a thickness of $d = 3$ nm is divided into 75×75 cells with a 3 nm $\times$ 3 nm $\times$ 3 nm mesh. The energy density E contains exchange, PMA, Zeeman, demagnetization, and DMI energy terms. When we calculated demagnetization energy, the FFT algorithm with GPU acceleration is used for better efficiency.[59,60] Therefore, a long enough 2×10^5 Monte Carlo steps (MCS) were allowed to be adopted, ensuring that the global energy minimum is reached. The simulation details can be found in Section S4, Supporting Information. We first consider that the sample has a perpendicular magnetic anisotropy K_z ($K_z = K_{ux}^{eff} + \mu_0 M_s^2/2 \approx 7.8 \times 10^5$ J m^{-3}, where $M_s = 9 \times 10^5$ A m^{-1}). To include the additional uniaxial anisotropy in the film plane, we also consider an easy axis along y direction K_y ($K_y = K_{ux}^{eff} - K_{uy}^{eff} = 9.3 \times 10^4$ J m^{-3}). Compared to the circular skyrmion (**Figure 3**a) stabilized by isotropic DMI with $D_x = D_y = 2.215$ mJ m^{-2}, the relaxed skyrmion for the case with DMI anisotropy in the film plane ($D_x = 1.898$ mJ m^{-2}, $D_y = 2.215$ mJ m^{-2}) deforms into an elliptical shape with $a = 54$ nm and $b = 42$ nm, as shown in Figure 3b. Similarly, the in-plane uniaxial anisotropy K_y can also cause a deformation with $a = 186$ nm and $b = 54$ nm, as shown in Figure 3c. Therefore, these two anisotropies jointly facilitate the formation of elliptical skyrmions.

We now turn to reveal the microscopic origins of the anisotropic K_u^{eff} and DMI by investigating the microstructure and crystallinity using transmission electron microscopy (TEM) and X-ray diffraction (XRD). We prepared a wedged shape sample and a uniform sample with 50 nm thick Co layer under the same sputter conditions. In principle, the thin Co samples should have similar microstructures to the thick Co samples. For the cross section perpendicular to the wedge direction, the Co layer shows a disordered structure, as shown in **Figure 4**a. For the cross section parallel to the wedge direction, tilted columnar structures with an oblique angle of ≈33° are observed, as shown in Figure 4b. The comparison indicates that the in-plane structural symmetry about the xz plane is broken due to the oblique-angle deposition. XRD measurements were further performed to study the microstructures of the wedged and uniform samples. There is a broad peak at ≈44.74° for the uniform sample (blue dashed line in Figure 4c), corresponding to the hexagonal (002) plane of polycrystalline Co film (i.e., hcp-Co (002)).[61,62] For the wedged Co thin film, the peak position is located at ≈44.56° (red dashed lines in Figure 4d,e), no matter the X-ray incident plane is parallel (Figure 4d) or perpendicular (Figure 4e) to the wedge direction. It is noteworthy that the peaks of the two Si substrates are coincident at ≈69.12°.[61] Thus, the ≈0.18° shift of hcp-Co (002) peak results from structural change caused by the oblique-angle deposition. The left shift of the peak indicates that a tensile strain along c axis is formed during the oblique-sputtering process. Accordingly, a compressive strain with an estimated amplitude of ≈0.38% (see Section S6, Supporting Information) is expected to form in the film plane. Based on the different cross section structures parallel and perpendicular to the wedge direction, we speculate that the strain in the film plane is anisotropic, which is the origins of the anisotropic K_u^{eff} and DMI in the film plane.

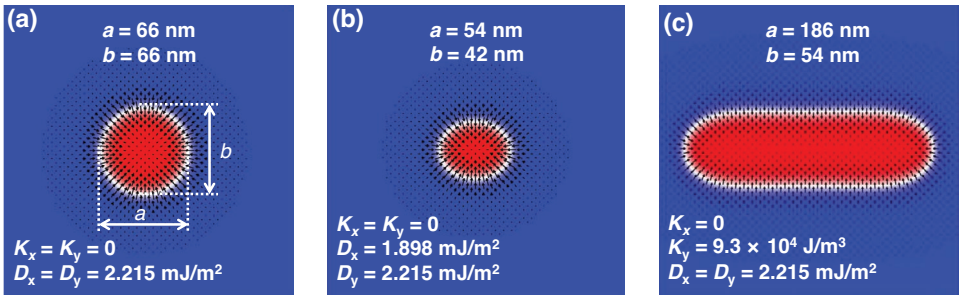

Figure 3. a) Simulation results in isotropic K_u^{eff} and DMI (i.e., $K_x = K_y$ and $D_x = D_y$) in the film plane. b,c) The deformation of skyrmion under anisotropic DMI (b) and in-plane uniaxial anisotropy (c) respectively. The red (blue) color represents magnetizations pointing in $+z$ ($-z$) direction.

© 2021 Wiley-VCH GmbH

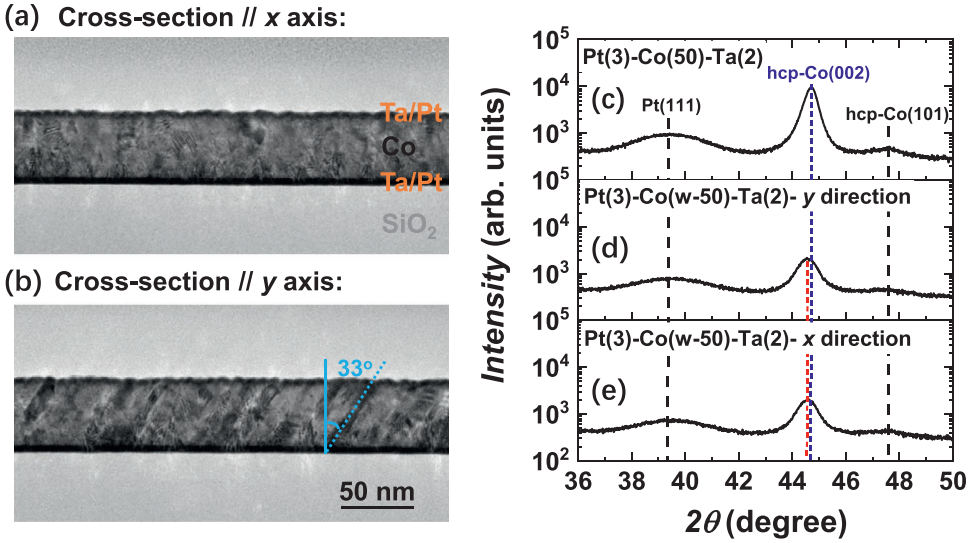

Figure 4. a,b) Cross-sectional TEM images for the cross section perpendicular (a) and parallel (b) to the wedge direction. The sample structure is Ta(2)/Pt(3)/Co(w-50)/Ta(2)/Pt(1) (thickness in nanometers), in which the 50 nm thick Co layer is grown by oblique-angle deposition. c–e) X-ray diffraction patterns for the uniform thin film of Ta(2)/Pt(3)/Co(50)/Ta(2)/Pt(1) (c) and wedged thin-film of Ta(2)/Pt(3)/Co(w-50)/Ta(2)/Pt(1) (d,e). For the wedged film, the X-ray incident plane is parallel (// *y* axis) (d) and perpendicular (// *x* axis) (e) to the wedge direction, respectively.

To confirm our conjecture, first-principles calculations are performed, and the detailed calculation method is shown in Section S5, Supporting Information. The structure of Co/Pt film and the applied in-plane strain are shown in **Figure 5**a,b (see details in Section S6, Supporting Information). The value of strain for the distorted structure is defined as $(b - a)/b$. For the calculations of microscopic and micromagnetic DMI between two nearest neighbors of Co atoms along axis *a* (*b*) (indicated by d_a (d_b) and D_a, (D_b)) as shown in Figure 5c,d, we use the chirality-dependent total energy difference approach applied previously for Co/Pt structures and Co/graphene.[63,64] The positive signs of d_a and d_b indicate that Co/Pt film prefers anticlockwise DMI. As shown in Figure 5c,d, the DMI of the pristine Co/Pt film is isotropic with a value of 3.02 meV, which is in agreement

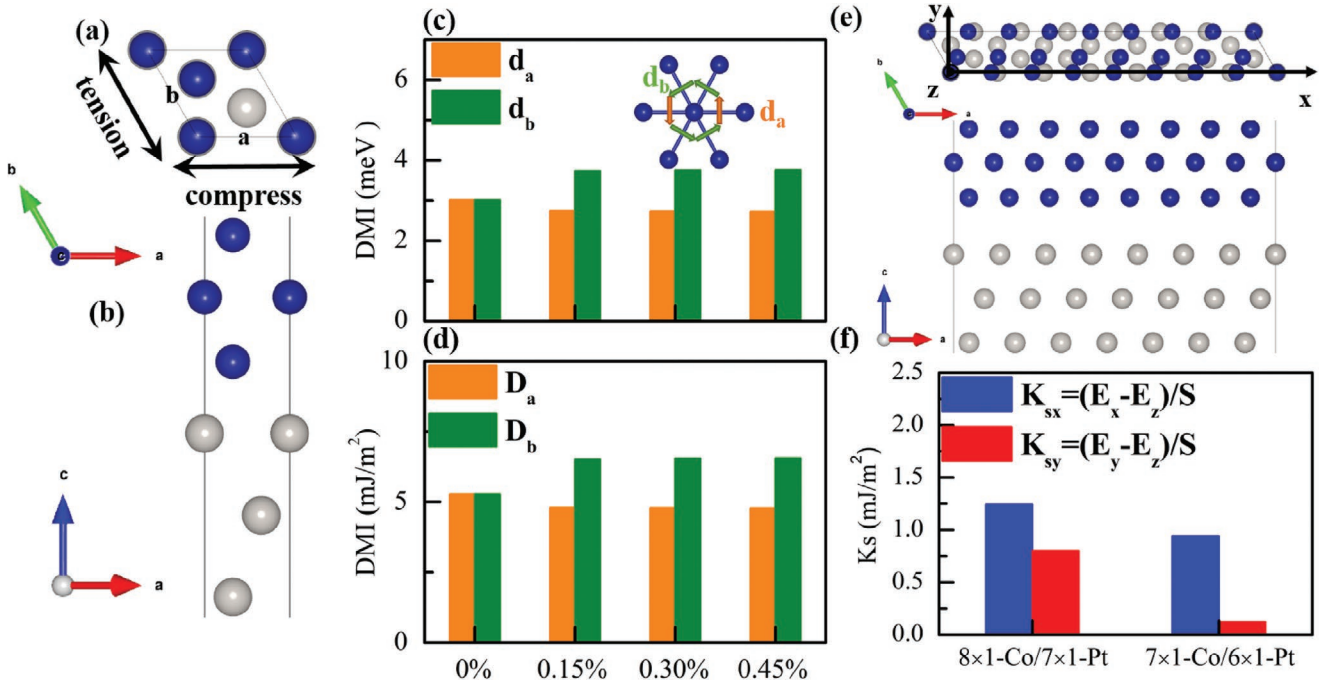

Figure 5. a) Top and b) side views of the pristine Co/Pt structure. The compression is applied along *a* axis and the corresponding tension is along *b* axis. The volume is kept as a constant. c) Microscopic DMI coefficients d_a (orange), d_b (olive) and d) micromagnetic DMI coefficients D_a (orange), D_b (olive) as a function of in-plane strain. e) The top and side view of 8 × 1-Co/7 × 1-Pt structure. f) Interfacial anisotropy K_s for the films along *x* and *y* axes K_{sx} (blue) and K_{sy} (red) values with different mismatched Co/Pt films.

© 2021 Wiley-VCH GmbH

with previous work.[63] However, the DMI between two nearest neighboring Co atoms along axis *a*, d_a and along axis *b*, d_b are anisotropic when the distortion is applied as summarized in Figure 5c. The amplitude of d_a decreases when the lattice along axis *a* is compressed, while d_b increases simultaneously due to the elongated lattice along axis *b*. Our results demonstrate that a small strain can induce a large DMI anisotropy, and this DMI anisotropy will keep almost as a constant for the strain in the range of 0.15% and 0.45%. Besides, the DMI along different directions under large strain about 1.5%, 3.0%, and 4.5% have also been studied in the same way. Interestingly, similar results are obtained (see Section S6, Supporting Information).

The magnetic anisotropy of Co/Pt film is also investigated. The pristine Co/Pt film has an isotropic out-of-plane interfacial anisotropy K_s of 0.701 mJ m^{-2}. PMA is defined as the energy difference between in-plane and out-of-plane magnetizations. Here, we only consider three Co monolayers (MLs), and define K_s for the film along *x* and *y* axes as K_{sx} and K_{sy}. To introduce the in-plane strain in the calculation, we built two mismatched Co/Pt films (Section S6, Supporting Information): 7 × 1-Co/6 × 1-Pt and 8 × 1-Co/7 × 1-Pt. Analogous to DMI, the PMA is also anisotropic under in-plane strain. The in-plane easy axis is along *y* axis, as depicted in Figure 5e. Figure 5f shows that, for the mismatched structure 8 × 1-Co/7 × 1-Pt, the difference between K_{sx} and K_{sy} is 0.441 mJ m^{-2}; while for the mismatched structure 7 × 1-Co/6 × 1-Pt, the different value increases to 0.820 mJ m^{-2}. Moreover, we obtain the difference of shape anisotropy along *x* and *y* axes about 0.02 mJ m^{-2}, which is much smaller than the difference of K_s, indicating that the experimentally observed anisotropic K_u^{eff} is caused by the in-plane strain-induced difference of K_s along different axes in thin Co/Pt film.

Recent studies show that spin wave modes and skyrmion Hall effect (SkHE) can be tuned by the shape of the skyrmion.[30,65] Especially, the tunability of the shape of skyrmion proposes a new degree of freedom that enables the elimination of SkHE.[30] Besides, magnetic antiskyrmions as topologically nontrivial chiral spin quasiparticles that are now found in several tetragonal Heusler materials.[66,67] Meanwhile, the anisotropic DMI with opposite signs along two orthogonal in-plane directions are responsible for the stabilization of the magnetic antiskyrmions. Our results present an approach to the realization of anisotropic DMI, which would make the implementation of the antiskyrmions possible in magnetic multilayers.

In summary, we observed elliptical magnetic skyrmions in asymmetric multilayer structure. The formation of elliptical skyrmions is ascribed to the anisotropic effective perpendicular magnetic K_u^{eff} and DMI in the film plane as confirmed by the Monte Carlo simulations with the standard Metropolis algorithm. Furthermore, the structural analysis and first-principles calculations reveal that the anisotropic K_u^{eff} and DMI are originated from the anisotropic strain in the film plane due to the oblique-angle deposition. Our method can be employed for tuning the morphology of skyrmions and can be useful for the realization of antiskyrmion in magnetic multilayers via engineering the anisotropic DMI. This study provides a new avenue for the engineering of skyrmionic devices with tuneable skyrmion dynamics due to the unusual dynamical characteristics of elliptical magnetic skyrmions.[27–30]

Experimental Section

Sample Growth: The multilayers were deposited by the magnetron sputtering method at room temperature on a thermally oxidized Si/SiO_2 substrate under the base pressure lower than 5×10^{-8} Torr. The substrates keep rotating during the deposition except for the Co layer. The Co layer was deposited by oblique angle deposition and thus had a wedge shape. A 1 nm Pt capping layer was deposited on the top to avoid the films to be oxidized.

Magnetic Properties Measurement: The magnetic properties were measured by the magnetic transport measurement system, Evico magneto-optic Kerr microscope, and SQUID (Quantum Design) magnetometer. The magnetic domains and skyrmions were measured by an Evico magneto-optic Kerr microscope.

Structural Analysis: The structures of the multilayers were characterized by the XRD and the TEM.

Supporting Information

Supporting Information is available from the Wiley Online Library or from the author.

Acknowledgements

Financial support from the National Natural Science Foundation of China (NSFC, grants nos. 11874409, 51671098, 91963201, and 11874059), Beijing Natural Science Foundation (grant no. Z190009), the Strategic Priority Research Program (B) (grant no. XDB07030200), the Key Research Program of Frontier Sciences (grant no. QYZDJ-SSW-SLH016 and ZDBS-LY-7021), Science Center of the National Science Foundation of China (No. 52088101), the NSFC-Science Foundation Ireland (SFI) Partnership Programmer (grant no. 51861135104), K. C. Wong Education Foundation (GJTD-2019-14), China Postdoctoral Science Foundation (no. 2020M670499), the 111 Project (no. B20063), and grant no. KQTD20180413181702403 is acknowledged. Y.L. acknowledges the support by the Special Postdoctoral Researchers Program of RIKEN.

Conflict of Interest

The authors declare no conflict of interest.

Data Availability Statement

The data that support the findings of this study are available on request from the corresponding author. The data are not publicly available due to privacy or ethical restrictions.

Keywords

anisotropic strain, Dzyaloshinskii–Moriya interaction anisotropy, elliptical skyrmions, magnetic anisotropy

Received: October 12, 2020
Revised: January 10, 2021
Published online: February 18, 2021

[1] A. Fert, V. Cros, J. Sampaio, *Nat. Nanotechnol.* **2013**, *8*, 152.
[2] N. Nagaosa, Y. Tokura, *Nat. Nanotechnol.* **2013**, *8*, 899.
[3] W. Jiang, X. Zhang, G. Yu, W. Zhang, X. Wang, M. B. Jungfleisch, J. E. Pearson, X. Cheng, O. Heinonen, K. L. Wang, Y. Zhou, A. Hoffmann, S. G. E. te Velthuis, *Nat. Phys.* **2016**, *13*, 162.

 © 2021 Wiley-VCH GmbH

[4] A. Fert, N. Reyren, V. Cros, *Nat. Rev. Mater.* **2017**, *2*, 17031.
[5] I. Dzyaloshinsky, *J. Exp. Theor. Phys.* **1957**, *5*, 1259.
[6] T. Moriya, *Phys. Rev.* **1960**, *120*, 91.
[7] A. Fert, P. M. Levy, *Phys. Rev. Lett.* **1980**, *44*, 1538.
[8] M. Bode, M. Heide, K. von Bergmann, P. Ferriani, S. Heinze, G. Bihlmayer, A. Kubetzka, O. Pietzsch, S. Blugel, R. Wiesendanger, *Nature* **2007**, *447*, 190.
[9] M. Heide, G. Bihlmayer, S. Blügel, *Phys. Rev. B* **2008**, *78*, 140403.
[10] G. Chen, J. Zhu, A. Quesada, J. Li, A. T. N'Diaye, Y. Huo, T. P. Ma, Y. Chen, H. Y. Kwon, C. Won, Z. Q. Qiu, A. K. Schmid, Y. Z. Wu, *Phys. Rev. Lett.* **2013**, *110*, 177204.
[11] S. Mühlbauer, B. Binz, F. Jonietz, C. Pfleiderer, A. Rosch, A. Neubauer, R. Georgii, P. Böni, *Science* **2009**, *323*, 915.
[12] A. Neubauer, C. Pfleiderer, B. Binz, A. Rosch, R. Ritz, P. G. Niklowitz, P. Boni, *Phys. Rev. Lett.* **2009**, *102*, 186602.
[13] F. Jonietz, S. Muhlbauer, C. Pfleiderer, A. Neubauer, W. Munzer, A. Bauer, T. Adams, R. Georgii, P. Boni, R. A. Duine, K. Everschor, M. Garst, A. Rosch, *Science* **2010**, *330*, 1648.
[14] W. Münzer, A. Neubauer, T. Adams, S. Mühlbauer, C. Franz, F. Jonietz, R. Georgii, P. Böni, B. Pedersen, M. Schmidt, A. Rosch, C. Pfleiderer, *Phys. Rev. B* **2010**, *81*, 041203.
[15] X. Z. Yu, Y. Onose, N. Kanazawa, J. H. Park, J. H. Han, Y. Matsui, N. Nagaosa, Y. Tokura, *Nature* **2010**, *465*, 901.
[16] X. Z. Yu, N. Kanazawa, Y. Onose, K. Kimoto, W. Z. Zhang, S. Ishiwata, Y. Matsui, Y. Tokura, *Nat. Mater.* **2011**, *10*, 106.
[17] S. Seki, X. Z. Yu, S. Ishiwata, Y. Tokura, *Science* **2012**, *336*, 198.
[18] Y. Onose, Y. Okamura, S. Seki, S. Ishiwata, Y. Tokura, *Phys. Rev. Lett.* **2012**, *109*, 037603.
[19] W. Jiang, P. Upadhyaya, W. Zhang, G. Yu, M. B. Jungfleisch, F. Y. Fradin, J. E. Pearson, Y. Tserkovnyak, K. L. Wang, O. Heinonen, S. G. E. Velthuis, A. Hoffmann, *Science* **2015**, *349*, 283.
[20] G. Chen, A. Mascaraque, A. T. N'Diaye, A. K. Schmid, *Appl. Phys. Lett.* **2015**, *106*, 242404.
[21] O. Boulle, J. Vogel, H. Yang, S. Pizzini, D. de Souza Chaves, A. Locatelli, T. O. Mentes, A. Sala, L. D. Buda-Prejbeanu, O. Klein, M. Belmeguenai, Y. Roussigne, A. Stashkevich, S. M. Cherif, L. Aballe, M. Foerster, M. Chshiev, S. Auffret, I. M. Miron, G. Gaudin, *Nat. Nanotechnol.* **2016**, *11*, 449.
[22] G. Yu, P. Upadhyaya, X. Li, W. Li, S. K. Kim, Y. Fan, K. L. Wong, Y. Tserkovnyak, P. K. Amiri, K. L. Wang, *Nano Lett.* **2016**, *16*, 1981.
[23] S. Woo, K. Litzius, B. Kruger, M. Y. Im, L. Caretta, K. Richter, M. Mann, A. Krone, R. M. Reeve, M. Weigand, P. Agrawal, I. Lemesh, M. A. Mawass, P. Fischer, M. Klaui, G. S. Beach, *Nat. Mater.* **2016**, *15*, 501.
[24] C. Moreau-Luchaire, S. C. Mouta, N. Reyren, J. Sampaio, C. A. Vaz, N. Van Horne, K. Bouzehouane, K. Garcia, C. Deranlot, P. Warnicke, P. Wohlhuter, J. M. George, M. Weigand, J. Raabe, V. Cros, A. Fert, *Nat. Nanotechnol.* **2016**, *11*, 444.
[25] Y. Tokunaga, X. Z. Yu, J. S. White, H. M. Ronnow, D. Morikawa, Y. Taguchi, Y. Tokura, *Nat. Commun.* **2015**, *6*, 7638.
[26] K. Shibata, J. Iwasaki, N. Kanazawa, S. Aizawa, T. Tanigaki, M. Shirai, T. Nakajima, M. Kubota, M. Kawasaki, H. S. Park, D. Shindo, N. Nagaosa, Y. Tokura, *Nat. Nanotechnol.* **2015**, *10*, 589.
[27] J. Hagemeister, E. Y. Vedmedenko, R. Wiesendanger, *Phys. Rev. B* **2016**, *94*, 104434.
[28] P. J. Hsu, A. Kubetzka, A. Finco, N. Romming, K. Bergmann, R. Wiesendanger, *Nat. Nanotechnol.* **2017**, *12*, 123.
[29] T. Nagase, M. Komatsu, Y. G. So, T. Ishida, H. Yoshida, Y. Kawaguchi, Y. Tanaka, K. Saitoh, N. Ikarashi, M. Kuwahara, M. Nagao, *Phys. Rev. Lett.* **2019**, *123*, 137203.
[30] J. Xia, X. Zhang, M. Ezawa, Q. Shao, X. Liu, Y. Zhou, *Appl. Phys. Lett.* **2020**, *116*, 022407.
[31] W. Koshibae, N. Nagaosa, *Nat. Commun.* **2014**, *5*, 5148.
[32] W. Koshibae, N. Nagaosa, *Nat. Commun.* **2016**, *7*, 10542.
[33] A. K. Nayak, V. Kumar, T. Ma, P. Werner, E. Pippel, R. Sahoo, F. Damay, U. K. Rößler, C. Felser, S. S. P. Parkin, *Nature* **2017**, *548*, 561.
[34] M. Hoffmann, B. Zimmermann, G. P. Muller, D. Schurhoff, N. S. Kiselev, C. Melcher, S. Blugel, *Nat. Commun.* **2017**, *8*, 308.
[35] L. Peng, R. Takagi, W. Koshibae, K. Shibata, K. Nakajima, T. H. Arima, N. Nagaosa, S. Seki, X. Yu, Y. Tokura, *Nat. Nanotechnol.* **2020**, *15*, 181.
[36] J. Jena, B. Gobel, T. Ma, V. Kumar, R. Saha, I. Mertig, C. Felser, S. S. P. Parkin, *Nat. Commun.* **2020**, *11*, 1115.
[37] J. W. Lee, Y.-W. Oh, S.-Y. Park, A. I. Figueroa, G. van der Laan, G. Go, K.-J. Lee, B.-G. Park, *Phys. Rev. B* **2017**, *96*, 064405.
[38] C. Zhang, S. Fukami, K. Watanabe, A. Ohkawara, S. DuttaGupta, H. Sato, F. Matsukura, H. Ohno, *Appl. Phys. Lett.* **2016**, *109*, 192405.
[39] L. Liu, C.-F. Pai, Y. Li, H. Tseng, D. Ralph, R. Buhrman, *Science* **2012**, *336*, 555.
[40] T. Tanaka, H. Kontani, M. Naito, T. Naito, D. S. Hirashima, K. Yamada, J. Inoue, *Phys. Rev. B* **2008**, *77*, 165117.
[41] G. Yu, P. Upadhyaya, Y. Fan, J. G. Alzate, W. Jiang, K. L. Wong, S. Takei, S. A. Bender, L. T. Chang, Y. Jiang, M. Lang, J. Tang, Y. Wang, Y. Tserkovnyak, P. K. Amiri, K. L. Wang, *Nat. Nanotechnol.* **2014**, *9*, 548.
[42] B. Cui, H. Wu, D. Li, S. A. Razavi, D. Wu, K. L. Wong, M. Chang, M. Gao, Y. Zuo, L. Xi, K. L. Wang, *ACS Appl. Mater. Interfaces* **2019**, *11*, 39369.
[43] P. M. Chaikin, T. C. Lubensky, *Principles of Condensed-Matter Physics*, Cambridge University Press, Cambridge, UK **2000**.
[44] A. Thiaville, S. Rohart, É. Jué, V. Cros, A. Fert, *Europhys. Lett.* **2012**, *100*, 57002.
[45] S. Emori, U. Bauer, S.-M. Ahn, E. Martinez, G. S. Beach, *Nat. Mater.* **2013**, *12*, 611.
[46] M. Ezawa, *Phys. Rev. B* **2011**, *83*, 100408.
[47] S.-Z. Lin, *Phys. Rev. B* **2016**, *94*, 020402.
[48] L. Zhao, Z. Wang, X. Zhang, X. Liang, J. Xia, K. Wu, H. A. Zhou, Y. Dong, G. Yu, K. L. Wang, X. Liu, Y. Zhou, W. Jiang, *Phys. Rev. Lett.* **2020**, *125*, 027206.
[49] P. Metaxas, J. Jamet, A. Mougin, M. Cormier, J. Ferré, V. Baltz, B. Rodmacq, B. Dieny, R. Stamps, *Phys. Rev. Lett.* **2007**, *99*, 217208.
[50] S.-G. Je, D.-H. Kim, S.-C. Yoo, B.-C. Min, K.-J. Lee, S.-B. Choe, *Phys. Rev. B* **2013**, *88*, 214401.
[51] A. Hrabec, N. Porter, A. Wells, M. Benitez, G. Burnell, S. McVitie, D. McGrouther, T. Moore, C. Marrows, *Phys. Rev. B* **2014**, *90*, 020402.
[52] R. Soucaille, M. Belmeguenai, J. Torrejon, J. V. Kim, T. Devolder, Y. Roussigné, S. M. Chérif, A. A. Stashkevich, M. Hayashi, J. P. Adam, *Phys. Rev. B* **2016**, *94*, 104431.
[53] D.-Y. Kim, M.-H. Park, Y.-K. Park, J.-S. Yu, J.-S. Kim, D.-H. Kim, B.-C. Min, S.-B. Choe, *Appl. Phys. Lett.* **2018**, *112*, 062406.
[54] C.-F. Pai, M. Mann, A. J. Tan, G. S. D. Beach, *Phys. Rev. B* **2016**, *93*, 144409.
[55] V. Mohanan, K. R. Ganesh, P. S. Anil Kumar, *Phys. Rev. B* **2017**, *96*, 104412.
[56] J. Yun, D. Li, B. Cui, X. Guo, K. Wu, X. Zhang, Y. Wang, J. Mao, Y. Zuo, L. Xi, *J. Phys. D: Appl. Phys.* **2018**, *51*, 155001.
[57] D. P. Landau, K. Binder, *A Guide to Monte Carlo Simulations in Statistical Physics*, Cambridge University Press, New York **2009**.
[58] D. Yu, S. Luo, Y. Li, V. Koval, C. Jia, *Phys. Rev. B* **2019**, *100*, 104410.
[59] N. Hayashi, K. Saito, A. Y. Nakatani, *Jpn. J. Appl. Phys.* **1996**, *35*, 6065.
[60] D. Yu, J. Kang, J. Berakdar, C. Jia, *NPG Asia Mater.* **2020**, *12*, 36.
[61] K. Vahaplar, S. Tari, H. Tokuc, S. Okur, *J. Vac. Sci. Technol., B: Microelectron. Nanometer Struct.–Process., Meas., Phenom.* **2009**, *27*, 2112.

© 2021 Wiley-VCH GmbH

[62] M. Paladini, V. Godinho, G. M. Arzac, M. C. Jiménez de Haro, A. M. Beltrán, A. Fernández, *RSC Adv.* **2016**, *6*, 108611.
[63] H. Yang, A. Thiaville, S. Rohart, A. Fert, M. Chshiev, *Phys. Rev. Lett.* **2015**, *115*, 267210.
[64] H. Yang, G. Chen, A. A. C. Cotta, A. T. N'Diaye, S. A. Nikolaev, E. A. Soares, W. A. A. Macedo, K. Liu, A. K. Schmid, A. Fert, M. Chshiev, *Nat. Mater.* **2018**, *17*, 605.
[65] Y. Liu, R. K. Lake, J. Zang, *J. Magn. Magn. Mater.* **2018**, *455*, 9.
[66] A. K. Nayak, V. Kumar, T. Ma, P. Werner, E. Pippel, R. Sahoo, F. Damay, U. K. Rossler, C. Felser, S. S. P. Parkin, *Nature* **2017**, *548*, 561.
[67] S. Sen, C. Singh, P. K. Mukharjee, R. Nath, A. K. Nayak, *Phys. Rev. B* **2019**, *99*, 134404.

© 2021 Wiley-VCH GmbH